Variations in the fundamental constants in the QSO host J1148+5251 at $z = 6.4$ and the BR1202−0725 system at $z = 4.7$

L. Lentati,[1]⋆ C. Carilli,[2] P. Alexander,[1] R. Maiolino,[1,3] R. Wang,[2] P. Cox,[4]
D. Downes,[4] R. McMahon,[3,5] K. M. Menten,[6] R. Neri,[4] D. Riechers,[7] J. Wagg,[1,8]
F. Walter[9] and A. Wolfe[10]

[1]*Astrophysics Group, Cavendish Laboratory, JJ Thomson Avenue, Cambridge, CB3 0HE, UK*
[2]*National Radio Astronomy Observatory, PO Box O, Socorro, NM 87801, USA*
[3]*Kavli Institute for Cosmology, University of Cambridge, Madingley Road, Cambridge CB3 0HA, UK*
[4]*Institut de Radio Astronomie Millimetrique, 300 Rue de la Piscine, Domaine Universitaire, 38406 Saint Martin d'Héres, France*
[5]*Institute of Astronomy, University of Cambridge, Madingley Road, Cambridge, CB3 0HA, UK*
[6]*Max-Planck-Institut für Radioastronomie, Auf dem Hügel 69, D-53121 Bonn, Germany*
[7]*Astronomy Department, California Institute of Technology, MC 249-17, 1200 East California Boulevard, Pasadena, CA 91125, USA*
[8]*European Southern Observatory, Alonso de Cordova 3107, Vitacura, Casilla 19001, Santiago 19, Chile*
[9]*Max-Planck-Institut für Astronomie, Königstuhl 17, D-69117 Heidelberg, Germany*
[10]*Department of Physics, Centre for Astrophysics & Space Sciences, University of California, San Diego, CA 92093, USA*

ABSTRACT

We use sensitive observations of three high-redshift sources: [C II] $^2P_{3/2} \rightarrow {}^2P_{1/2}$ fine-structure and CO ($J = 2 \rightarrow 1$) rotational transitions for the $z = 6.4$ quasar (QSO) host galaxy J1148+5251 taken with the Plateau de Bure Interferometer (PdBI) and Jansky Very Large Array, respectively, and [C II] and CO ($J = 5 \rightarrow 4$) transitions from the QSO BR1202−0725 and its companion sub-millimetre galaxy (SMG) at $z = 4.7$ taken with the Atacama Large Millimeter Array and the PdBI. We use these observations to place constraints on the quantity $\Delta z = z_{CO} - z_{C II}$ for each source where z_{CO} and $z_{C II}$ are the observed redshifts of the CO rotational transition and [C II] fine-structure transition, respectively, using a combination of approaches: (1) modelling the emission line profiles using 'shapelets' – a complete orthonormal set of basis functions that allow us to recreate most physical line shapes – to compare both the emission redshifts and the line profiles themselves, in order to make inferences about the intrinsic velocity differences between the molecular and atomic gas, and (2) performing a marginalization over all model parameters in order to calculate a non-parametric estimate of Δz. We derive 99 per cent confidence intervals for the marginalized posterior of Δz of $(-1.9 \pm 1.3) \times 10^{-3}$, $(-3 \pm 8) \times 10^{-4}$ and $(-2 \pm 4) \times 10^{-3}$ for J1148+5251, and the BR1202−0725 QSO and SMG, respectively. We show that the [C II] and CO ($J = 2 \rightarrow 1$) line profiles for J1148+5251 are consistent with each other within the limits of the data, whilst the [C II] and CO ($J = 5 \rightarrow 4$) line profiles from the BR1202−0725 QSO and SMG, respectively, have 65 and >99.9 per cent probabilities of being inconsistent, with the CO ($J = 5 \rightarrow 4$) lines ∼30 per cent wider than the [C II] lines. Therefore, whilst the observed values of Δz can correspond to variations in the quantity $\Delta F/F$ with cosmic time, where $F = \alpha^2/\mu$, with α the fine-structure constant and μ the proton-to-electron mass ratio, of both $(-3.3 \pm 2.3) \times 10^{-4}$ for a look-back time of 12.9 Gyr and of $(-5 \pm 15) \times 10^{-5}$ for a look-back time of 12.4 Gyr, we propose that they are the result of the two species of gas being spatially separated as indicated by the inconsistencies in their line profiles.

Key words: line: profiles – methods: data analysis – quasars: emission lines – cosmology: observations.

⋆ E-mail: ltl21@cam.ac.uk

1 INTRODUCTION

One of the most important principles that underlie much of modern physics is that of *Copernicus*; that our location in space and time is not special, such that the laws of physics do not change from one point in space–time to another. All these laws contain within them a relationship to the fundamental constants; electromagnetic interactions involve the fine-structure constant α, gravitational interactions depend on the gravitational constant G and so on. It is therefore a natural question to ask whether these constants are constant with cosmic epoch.

This question is not a new one, being proposed some 70 years ago by Dirac (1937) and Milne (1935). Since then however it has become of particular interest with the development of physical models that seek to unify the fundamental forces via extra dimensions, such as Kaluza–Klein, or superstring theories. For a recent review, both of the theoretical models that allow for variations in the fundamental constants, and constraints placed on the variations by both terrestrial and astrophysical methods, see Uzan (2011). Below we will describe only in brief what is needed to aid further discussion.

In short, the extra dimensions predicted by these theories would have only manifested themselves in the first instant of time following the big bang ($\sim 10^{-43}$ s, or energies of $\sim 10^{19}$ GeV) before compactifying to the Planck scale during the cosmic expansion that followed. Over cosmic time variations in the scale factors of these now compactified extra dimensions could manifest themselves physically in our 4D Universe as an evolution of the fundamental constants, and as such a measurement showing any such evolution could provide supporting evidence for the existence of these compact dimensions.

Astrophysical methods used to acquire constraints on the fundamental constants are based on comparing the differences between the observed line centres of absorption or emission lines from astrophysical sources, to their expected values in a laboratory frame on Earth. A wide range of different atomic and molecular transitions have been used for this purpose, examples of which include comparisons between the inversion line NH_3 and rotational lines from CS and H_2CO which resulted in the current best constraints on $\Delta\mu/\mu$ of -3.5×10^{-7} from $z \sim 0.685$ to the present (Kanekar 2011), whilst limits on the evolution of α of $\Delta\alpha/\alpha = (-1.5 \pm 2.6) \times 10^{-6}$ have been set using Si II and Fe II absorption lines from a $z = 1.5$ quasar (QSO; Agafonova et al. 2011) and of $\Delta\alpha/\alpha = (-1.7 \pm 1.4) \times 10^{-6}$ using the combination of H I and OH lines from a $z = 0.765$ absorption system (Kanekar et al. 2012). Evidence for a spatial variation in the fine-structure constant has also been presented (Webb et al. 2011; King et al. 2012), with the variation fitting a dipole with a significance at the 4.2σ level, in the direction right ascension $17^{\mathrm{h}}5 \pm 0^{\mathrm{h}}9$, declination $-58° \pm 9°$.

In Levshakov et al. (2008) a method was proposed to compare the redshifts of far-infrared (FIR) fine-structure lines and low-lying rotational transitions of the CO molecule. This combination is sensitive to variations in the combined quantity $F = \alpha^2/\mu$.

The advantage of FIR fine-structure lines is that they are approximately 30 times more sensitive to variations in α than optical and UV transitions. In particular, the fine-structure transition of singly ionized carbon $^2P_{3/2} \rightarrow {}^2P_{1/2}$ has the combined benefit of providing excellent sensitivity as well as intrinsically being one of the brightest emission lines found in star-forming galaxies (e.g. Crawford et al. 1985; Stacey et al. 1991).

CO transitions then provide a second independent value for the redshift of the source. The frequencies of these emission lines are

dependent on μ such that by calculating the quantity $\Delta z = z_{\mathrm{rot}} - z_{\mathrm{fs}}$ leads to the combined quantity F:

$$\frac{\Delta z}{1 + z_{\mathrm{avg}}} = \frac{\Delta F}{F}, \tag{1}$$

where z_{avg} is the weighted average of available redshift measurements.

This method has been used for high-redshift sources to place constraints on $\Delta F/F$. For example, in a $z = 5.2$ system Levshakov et al. (2012) place limits of $\Delta F/F < 2 \times 10^{-5}$ using the CO ($J = 7 \rightarrow 6$) rotational transition combined with the [C I] $^3P_2 \rightarrow {}^3P_1$ fine-structure transition.

Here we apply this method to the analysis of three systems. Using the CO ($J = 2 \rightarrow 1$) rotational transition and the [C II] $^2P_{3/2} \rightarrow {}^2P_{1/2}$ fine-structure transition from the $z = 6.4$ QSO J1148+5251 and from the $z = 4.7$ QSO BR1202−0725 and its companion submillimetre galaxy (SMG) using the CO ($J = 5 \rightarrow 4$) rotational transition and the above [C II] line, we derive values of $\Delta F/F$.

We do this first following a traditional approach where we fit a single parametrized model to both emission lines for a given system and compare the line centroids to determine values of Δz. Due to the very high signal-to-noise ratio in some of the observations, however, it becomes increasingly possible, and important, to account for the non-Gaussian features in a line profile. We therefore take the approach of modelling the line profiles using shapelets, which provide a powerful way of describing any physical line shape by expressing it in terms of a particular orthonormal basis. We thus take the approach that, whilst the emission lines from a particular system might not be perfectly Gaussian, if the emission is co-located spatially, then they should share the same non-Gaussian traits.

By performing our analysis using the principles of Bayesian inference, we can determine the optimal number of shapelet basis functions required to properly describe the data, and because the zeroth-order shapelet is a Gaussian itself we include that as a possible model against which to compare others implicitly.

We also present a second, non-parametric method of analysing the spectral data. Using the Bayesian approach, we are able to not only quantify objectively the probability that two emission lines from the same source share the same line shape, but by marginalizing over the coefficients for all possible models, we calculate the posterior probability distribution for $\Delta F/F$ independent of any particular choice of model.

In Section 2, we describe the observations used in this analysis. In Section 3, we describe the basic mathematical framework behind shapelets, their application to our data and the marginalization process. We present our results from all three systems in Section 4, and our discussion of these results along with our conclusions in Sections 5 and 6, respectively.

2 OBSERVATIONS

The observations of the [C II] line for J1148+5251 were made with the Plateau de Bure Interferometer (PdBI) in Maiolino et al. (2012) with a total on-source integration time of 17.5 h. We use channels smoothed to a width of 72 MHz with a noise level per channel of 0.79 mJy beam^{-1}. An aperture with diameter 4 arcsec was used to extract the spectra, resulting in a noise level per channel of 1.58 mJy and a total signal-to-noise ratio for the line of ~ 15. The CO ($J = 2 \rightarrow 1$) line was observed with the Jansky Very Large Array in 2011. Channel width was set to 8 MHz, and the noise per channel of 0.036 mJy beam^{-1} resulted in a total signal-to-noise ratio for the line of ~ 9. Both emission lines were imaged in a heliocentric

velocity frame; however, in order to present all the observations in this work in a single velocity frame we convert to local standard of rest (LSR) velocities by subtracting 10.27 km s^{-1}.

For a detailed description of the [C II] observations made of the two BR1202−0725 sources, see Wagg et al. (2012). To summarize, observations of the two lines were made with the Atacama Large Millimeter Array (ALMA) during 2012. The observations lasted 25 min and produced signal-to-noise ratios of ∼80 for both lines, an order of magnitude better than any previous sub-mm line or continuum observation of the system. The data are binned in channels ∼16 MHz wide for the QSO, and 32 MHz wide for the SMG, with noise levels per channel of 0.65 and 0.8 mJy beam^{-1}, respectively.

The CO ($J = 5 \rightarrow 4$) observations were made with the PdBI in 2007 February; for a detailed description refer to Salome et al. (2012). The channel width in both cases is ∼30 MHz, with noise per channel of 0.52 mJy, resulting in signal-to-noise ratios of ∼14 for both the QSO and SMG.

The PdBI observations were imaged in the LSR velocity frame, while the ALMA [C II] observations were made in a topocentric frame of reference; we therefore add 29 km s^{-1} to the [C II] observations in order to account for the difference between the two.

3 SHAPELETS

A thorough description of the Shapelet formalism can be found in Refregier (2003), with astronomical uses being described in e.g. Kelly & McKay (2004, 2005) and Refregier & Bacon (2003). Here we give only an outline to aid later discussion.

Shapelets are described by a set of dimensionless basis functions, which in one dimension can be written as

$$\phi_n(x) \equiv \left[2^n \sqrt{\pi} n! \right]^{-1/2} H_n(x)\, e^{-x^2/2}, \tag{2}$$

where n is a non-negative integer and H_n is the Hermite polynomial of order n. Therefore, the zeroth-order shapelet is given by a standard Gaussian ($H_0(x) = 1$), with higher order terms represented by a Gaussian multiplied by the relevant polynomial.

These are then modified by a scale factor β in order to construct the dimensional basis functions:

$$B_n(x; \beta) \equiv \beta^{-1/2} \phi_n(\beta^{-1} x), \tag{3}$$

the first five basis functions are shown in Fig. 1. These basis func-
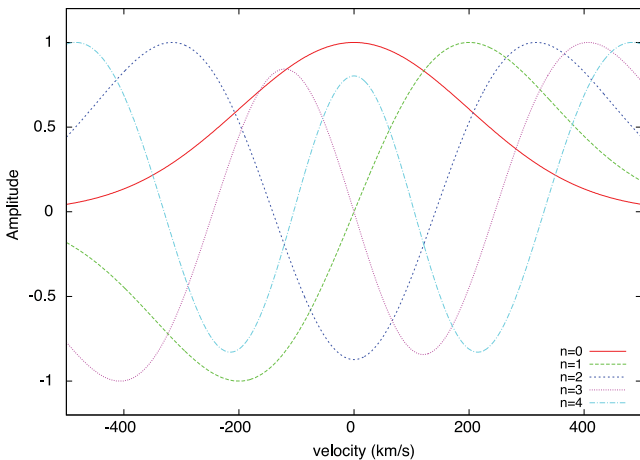

Figure 1. The first five 1D shapelet basis functions B_n. The scaling factor is set to 200 km s^{-1}, with amplitudes normalized such that each component has a maximum at 1 or minimum at −1. Note that the maxima/minima move further from the centre as n increases.

tions are orthonormal in that we can write

$$\int_{-\infty}^{\infty} dx\, B_n(x; \beta) B_m(x; \beta) = \delta_{mn}, \tag{4}$$

where δ_{mn} is the Kronecker delta so that we can represent a function $f(x)$ as

$$f(x) = \sum_{n=0}^{\infty} a_n B_n(x; \beta), \tag{5}$$

where a_n are shapelet coefficients. In practice, when dealing with discretely sampled data, this feature of orthonormality depends greatly on the positions of the sample points, the physical extent of the sample space with respect to the scaling factor β and the maximum number of basis vectors $n_{\max}$ used for reconstruction. For a discussion of this, see Berry, Hobson & Withington (2004). Due to the nature of our fitting process, we can calculate the orthonormality of the set of basis vectors used for every model. We then define the quantity $O_{\max}$ which describes the maximum deviation away from orthonormality for our basis vectors, i.e.

$$O_{\max} = \text{Max} \left[\left| 1 - \sum_{i=1}^{N_d} a_i^2 \right|, \left| 0 - \sum_{i=1}^{N_d} \sum_{j=1, j \neq i}^{N_d} a_i b_j \right| \right] \quad a, b \in \{n\} \tag{6}$$

and disregard any points where $O_{\max} > O_{\text{thresh}}$, where O_{thresh} is a threshold value for acceptance. We find that for values between 1 and 10 per cent, neither the individual best fits nor the marginalized result vary by more than 1 per cent. Below 1 per cent a large fraction of all solutions are rejected, and above 10–20 per cent the amount of power in non-orthogonal components can result in erroneous best fits. For the following work, we therefore set $O_{\text{thresh}} = 2$ per cent.

The total flux F_{tot} is given by

$$F_{\text{tot}} = \int_{-\infty}^{\infty} dx\, f(x) = \sum_{n}^{n=\text{even}} \left[2^{1-n} \pi^{1/2} \beta \right]^{1/2} \binom{n}{n/2}^{1/2}, \tag{7}$$

and the rms deviation of the function $f(x)$, σ_{m}, is given by

$$\sigma_{\text{m}}^2 = \int_{-\infty}^{\infty} dx\, x^2 f(x)$$
$$= \pi^{1/4} \beta^{\frac{5}{2}} F_{\text{tot}}^{-1} \sum_{n}^{n=\text{even}} 2^{1/2(1-n)} a_n (1 + 2n) \binom{n}{n/2}^{1/2}. \tag{8}$$

We use this definition of the rms radius to define the full width at half-maximum (FWHM) of a particular line shape as $2.3548\sigma_{\text{m}}$.

3.1 Determining the optimal number of shapelet coefficients

In fitting a shapelet model to an observed spectrum using a set of n coefficients, we would like to be able to determine the optimal n that the data can support, a task for which Bayesian inference is ideal. Using the MULTINEST algorithm (Feroz, Hobson & Bridges 2009), we are able to analyse efficiently spectral data containing individual or multiple emission lines, where the Bayesian evidence returned by the algorithm can be used to objectively perform model selection between different numbers of coefficients.

The Bayesian evidence for a set of n parameters Θ is given by the integral of the likelihood $L(\Theta)$ multiplied by the prior $\pi(\Theta)$ across the whole parameter space:

$$E = \int L(\Theta) \pi(\Theta)\, d^n \Theta. \tag{9}$$

The evidence is larger for a model if more of its parameter space is likely and smaller for a model with large areas in its parameter

space having low likelihood values, even if the likelihood function is very highly peaked. Thus, the evidence automatically implements Occam's razor: a simpler theory with a compact parameter space will have a larger evidence than a more complicated one, unless the latter is significantly better at explaining the data. The question of model selection between two models H_0 and H_1 can then be answered by comparing their evidences E_0 and E_1 by calculating the ratio R:

$$R = \frac{E_1}{E_0}, \tag{10}$$

which then gives us the probability that the model H_1 is supported by the data compared to H_0 by

$$P = \frac{R}{1 + R}. \tag{11}$$

In this paper we consider the following scenarios.

(i) We have two emission lines and fit two independent models using the parameters ν_i, β_i, C_i and a set of n_i shapelet coefficients. Here ν is the central frequency, β is the scaling parameter, C is a continuum component, n represents the set of shapelet coefficients used in the model and the subscript $i = 1, 2$ refers to the particular emission line.

(ii) We have two emission lines and fit a joint model using the parameters ν_1, ν_2, β, C, α and a set of n shapelet coefficients. Here ν_1 and ν_2 are the central frequencies of the two emission lines which are allowed to vary independently, whilst β, the scaling parameter, C, a continuum component, and n, the set of shapelet coefficients used in the model, are the same for both emission lines. Finally, α is an amplitude scaling parameter representing the ratio of the two line peaks.

By comparing the Bayesian evidence for these two scenarios, we are therefore able to objectively determine whether the two line shapes are consistent with one another within the limits provided by the data. In both these cases, we also determine values of the redshift associated with the central frequencies of the emission lines, and in those cases where we fit the joint model we calculate $\Delta z = z_{CO} - z_{C II}$, and $\Delta F/F$ for the model, and the errors associated with these quantities.

The only constraint that we place on the line shapes produced by the shapelet coefficients is that they must be positive for all values of velocity. We therefore reject all points that have any negative amplitudes by subtracting a large value from their log likelihood when a negative amplitude is present.

3.2 Marginalizing over all possible line shapes

Whilst the advantages of a Bayesian approach are clear, in that we can robustly determine both the maximum number of model components supported by the data, and the coefficients that return the greatest Bayesian evidence, we are also able to marginalize over all the line shapes described by our shapelet coefficients in order to calculate the probability distribution of Δz alone.

The probability of a particular value of Δz resulting from model parameters $\boldsymbol{\theta}$ is given by

$$P(\Delta z, \boldsymbol{\theta}|\boldsymbol{D}) \propto \exp\left[-0.5(\boldsymbol{D} - \boldsymbol{M})^T \mathbf{N}^{-1}(\boldsymbol{D} - \boldsymbol{M})\right], \tag{12}$$

where $\boldsymbol{D}$ is our data vector, $\boldsymbol{M}$ is the vector containing the model described by the parameters $\boldsymbol{\theta}$ and $\mathbf{N}$ is the covariance matrix, which in all the following work we take to be diagonal, with elements $N_{ii} = \sigma_i^2$ where σ_i is the noise in channel i.

The probability of a particular value of Δz is therefore given by

$$P(\Delta z) = \int P(\boldsymbol{\theta}|\boldsymbol{D}) \, \mathrm{d}\boldsymbol{\theta}, \tag{13}$$

where we have integrated over all model parameters $\boldsymbol{\theta}$. In this way, we can account for the uncertainty in choosing a particular model, and may also include systems where the line shape is not well described by a Gaussian, as is the case for the SMG in the BR1202 system described in Section 4.3.

4 RESULTS

4.1 J1148+5251

4.1.1 Line profiles

The [C II] and CO ($J = 2 \rightarrow 1$) spectra for J1148+5251 are shown in Fig. 2. The evidence for the [C II] line supports a fit with $n_{max} = 7$ indicating large deviations from the $n = 0$ term (i.e. a single Gaussian). This can be seen in the spectrum as a set of extended wings originating from strong QSO outflows (Maiolino et al. 2012). The central Gaussian component has an FWHM of 306 ± 20 km s^{-1}, with an integrated flux of 7.5 Jy km s^{-1}. This represents 72 per cent of the total flux in the emission line, with 2.9 Jy km s^{-1}
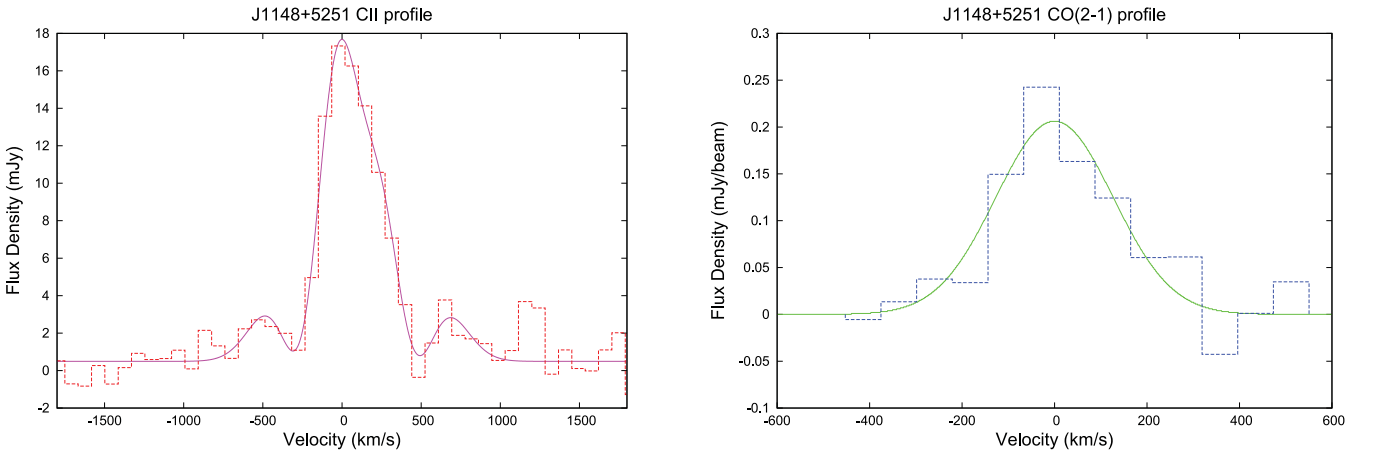
Figure 2. Left: [C II] spectrum (red) with the best-fitting model (magenta) overlaid. Right: CO ($J = 2 \rightarrow 1$) spectrum (blue) with the best-fitting model (green) overlaid for J1148+5251. In both cases, zero velocity is chosen to be at the peak of the respective model and not at a specific redshift value.

located in the non-Gaussian components. The total FWHM of the line model is 395 ± 30 km s^{-1}. We can compare this line width to the result of fitting only a single Gaussian model, which results in an FWHM of 400 ± 20 km s^{-1}. In contrast, the CO ($J = 2 \rightarrow 1$) line is adequately described by a single component model, with an FWHM of 297 ± 49 km s^{-1}. This is therefore consistent within 2σ errors with the C II line.

4.1.2 Performing a joint fit

As described in Section 3.1 when performing a joint fit we use only the velocity range that is shared between both data sets and as such we only fit for the joint profile out to edge of the CO data (approximately ± 500 km s^{-1}), which means that we exclude the majority of the extended wings seen in the [C II] profile from the fit. Fig. 3 (left) shows the best-fitting joint fit profile overlaid on to both the [C II] and CO ($J = 2 \rightarrow 1$) emission lines. The consistency between the line shapes can be described quantitatively by comparing the Bayesian evidence for a joint fit where the two lines are described by the same set of coefficients, and the evidence when the two lines are allowed to be described by different parameters. Here the log evidence supports a joint profile with a difference of 1.15, corresponding to a 76 per cent probability that the two emission lines are described by the same model within the limits of the data.

The joint fit is described by $n_{max} = 1$ and FWHM of 395 ± 24 km s^{-1}. Line centroids and redshifts are given in Table 1. We find $\Delta z = (-2.7 \pm 0.6 \times 10^{-3})$, which, if the difference in redshifts were due only to changes in the fundamental constants and not the result of intrinsic differences in the line shape, would correspond to $\Delta F/F = (-3.6 \pm 0.8) \times 10^{-4}$, representing a 4.5σ deviation from zero. The separation in redshift is shown in Fig. 3 (right).

Fig. 4 shows the results of marginalizing over all model line profiles. The left-hand panel shows the normalized 2D probability distribution for n_{max} and Δz marginalized over all shapelet coefficients for that value of n_{max}. The peak is consistent with a value of $\Delta z \sim -2.4 \times 10^{-3}$ for all n_{max} with significant probabilities. Beyond this region, the probability distribution is zero to machine precision. The right-hand panel shows this 2D distribution marginalized over all n_{max}. The final result is consistent with a 99 per cent confidence interval for the value Δz of $(-2.4 \pm 1.7) \times 10^{-3}$.

Table 1. J1148+5251 emission line parameters from a joint fit.

Line	ν_{obs} (GHz)	z
[C II]	256.137 ± 0.010	6.4200 ± 0.0003
CO ($J = 2 \rightarrow 1$)	31.081 ± 0.002	6.4173 ± 0.0005

4.2 BR1202−0725 QSO component

4.2.1 Line profiles

The [C II] and CO ($J = 5 \rightarrow 4$) spectra for the BR1202 QSO are shown in Fig. 5. The [C II] emission line is best modelled by a single Gaussian with an FWHM of 290 ± 4 km s^{-1}, whilst the CO ($J = 5 \rightarrow 4$) line is described by a single Gaussian with an FWHM of 390 ± 30 km s^{-1}. As such the two profiles are not consistent with one another within their errors, with the CO emission line being ~ 30 per cent broader than the [C II] line.

4.2.2 Performing a joint fit

The difference in the line widths between the [C II] and CO ($J = 5 \rightarrow 4$) emission lines is demonstrated in the difference in the evidence values when comparing the joint fit to independent models, with a difference of approximately 0.5, corresponding to a 62 per cent probability that the two lines do not share the same line profile.

The joint fit is best described by a single Gaussian with an FWHM of 293 ± 6 km s^{-1} and is shown in Fig. 6 (left). Line centroids and redshifts are given in Table 2 and the separation in redshift is shown in Fig. 6 (right). From these we find values of $\Delta z = (-3 \pm 3) \times 10^{-4}$ and $\Delta F/F = -5 \pm 5 \times 10^{-5}$.

Since the evidence has a slight preference for independent models for the two lines, we also calculate values of Δz and $\Delta F/F$ for the two independently fitted models in order to see how large an effect underfitting the data with a single model can have on the result. In this case, the redshifts of the two emission lines are given by $z_{C II} = 4.694\,95 \pm 0.000\,03$ and $z_{CO} = 4.6948 \pm 0.0003$, which
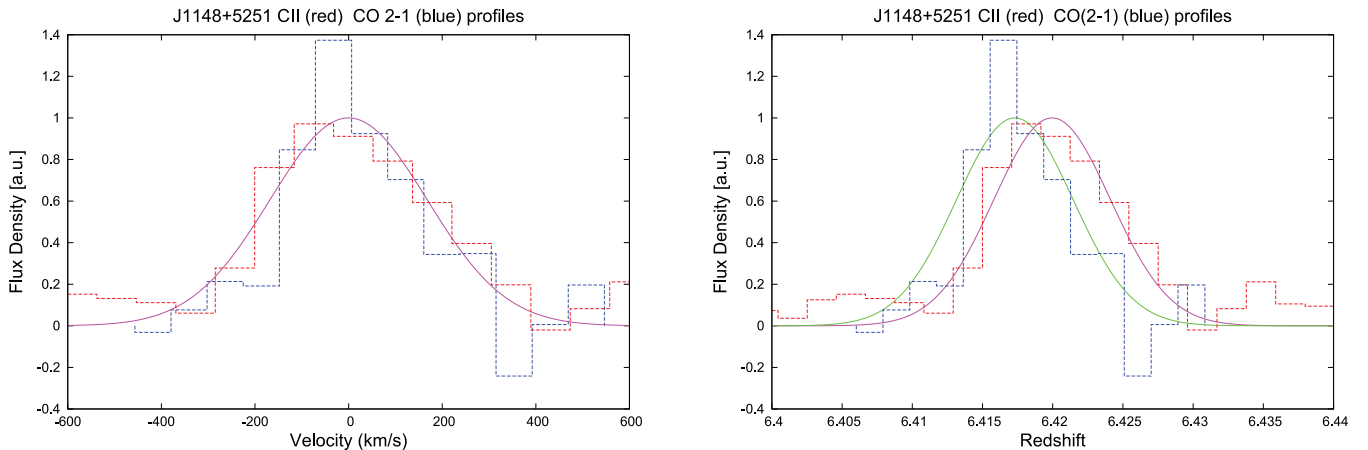

Figure 3. J1148+5251: (left) the best-fitting joint fit profile (magenta) overlaid on to both the [C II] (red dashed) and CO ($J = 2 \rightarrow 1$) (blue dashed) emission lines. Amplitudes have been normalized such that the model has a peak at 1.0, whilst the CO ($J = 2 \rightarrow 1$) and [C II] emission lines have peaks normalized such that their height relative to the model is as in the best fit. Both emission lines are shown with zero velocity corresponding to their model redshift. Right: [C II] data (red dashed line) and CO ($J = 2 \rightarrow 1$) data (blue dashed line) on a redshift axis with amplitudes normalized as in the left-hand panel. Redshifts have been calculated using rest-frame emission frequencies of 1900.539 and 230.538 GHz for the [C II] and CO lines, respectively. The solid magenta and green lines denote the joint fit model line profiles at their best-fitting redshift values for the [C II] and CO ($J = 2 \rightarrow 1$) lines, respectively.
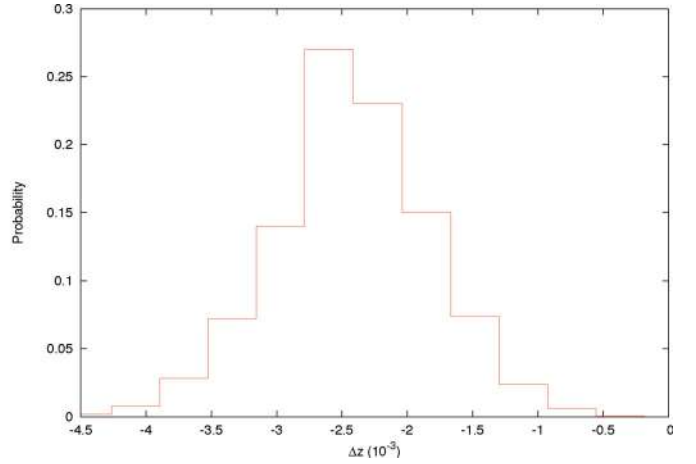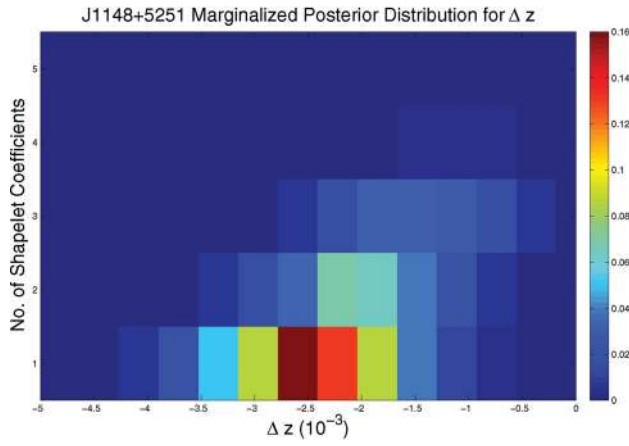
Figure 4. Left: normalized 2D probability distribution for n_{max} and $\Delta F/F$ marginalized over shapelet coefficients. Right: normalized 1D probability distribution for $\Delta F/F$ marginalized over all n_{max} and all shapelet coefficients.
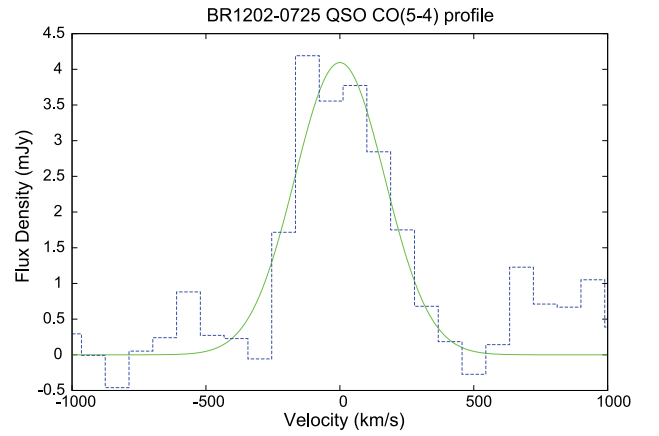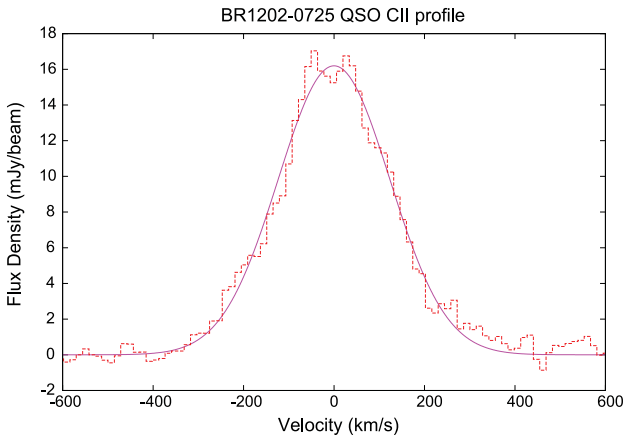

Figure 5. BR1202−0725: (left) the [C II] spectrum (red) with the best-fitting model (magenta) overlaid. Right: CO ($J = 5 \rightarrow 4$) spectrum (blue) with the best-fitting model (green) overlaid. In both cases, zero velocity is chosen to be at the peak of the respective model and not at a specific redshift value.
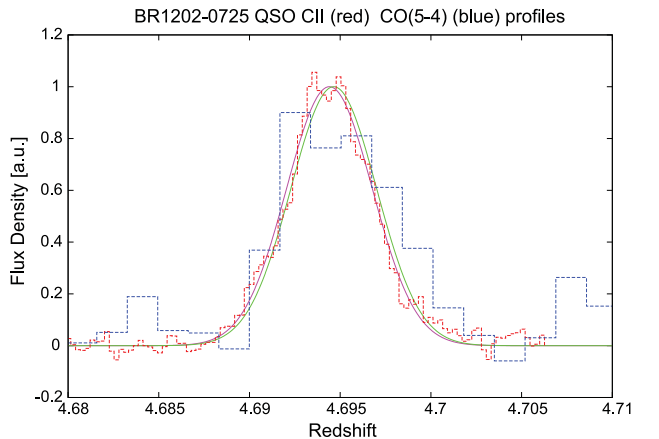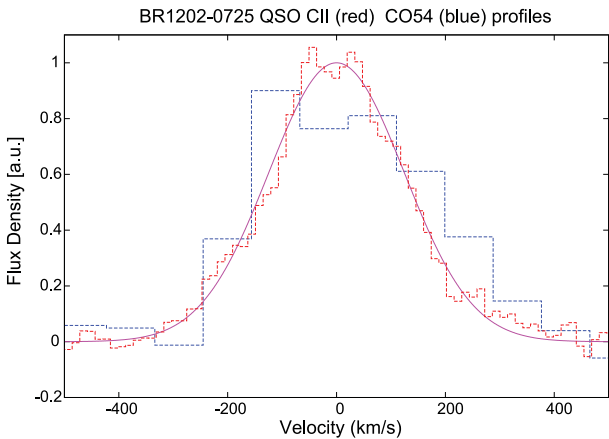

Figure 6. BR1202−0725: (left) the best-fitting joint fit profile (magenta line) overlaid on to both the [C II] (red dotted) and CO ($J = 5 \rightarrow 4$) (blue dotted) emission lines. Amplitudes have been normalized such that the model has a peak at 1.0, whilst the CO ($J = 5 \rightarrow 4$) and [C II] emission lines have peaks normalized such that their height relative to the model is as in the best fit. Both emission lines are shown with zero velocity corresponding to their model redshift. Right: [C II] data (red dashed line) and CO ($J = 5 \rightarrow 4$) data (blue dashed line) on a redshift axis with amplitudes normalized as in the left-hand panel. Redshifts have been calculated using rest-frame emission frequencies of 1900.539 and 576.267 931 GHz for the [C II] and CO lines, respectively. The solid magenta and green lines denote the joint fit model line profile at the best-fitting redshift values for the [C II] and CO ($J = 5 \rightarrow 4$) lines, respectively.
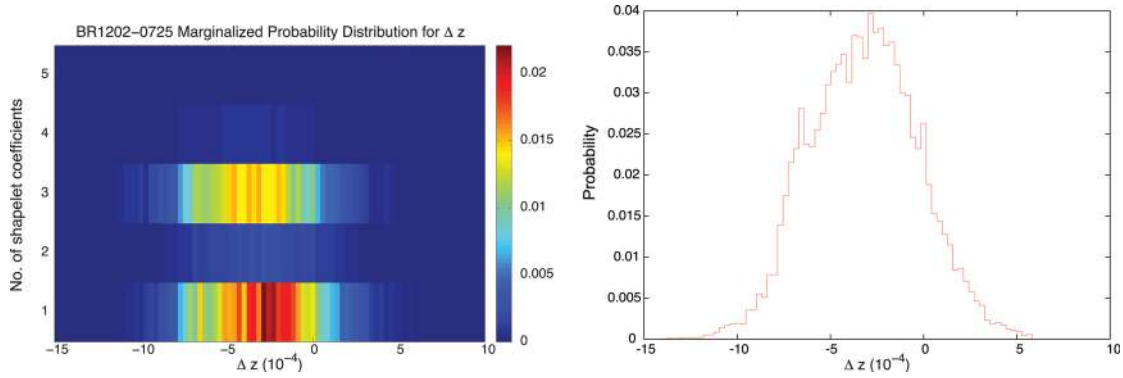
Figure 7. Left: normalized 2D probability distribution for n_{max} and Δz marginalized over shapelet coefficients. Right: normalized 1D probability distribution for Δz marginalized over all n_{max} and all shapelet coefficients.

Table 2. BR1202−0725 QSO emission line parameters from a joint fit.

Line	ν_{obs} (GHz)	z
[C II]	333.723 ± 0.002	$4.694\,96 \pm 0.000\,03$
CO $(5 \to 4)$	101.195 ± 0.005	4.6946 ± 0.0003

gives us $\Delta z = (-1.4 \pm 3) \times 10^{-4}$, and correspondingly $\Delta F/F = (-2 \pm 5) \times 10^{-5}$ if as before we assume that this difference in redshift is due only to an evolution in the fundamental constants.

Finally in Fig. 7 we show the marginalized posterior distribution Δz as for J1148+5251, from which we derive a 99 per cent confidence interval for Δz of $(-3 \pm 8) \times 10^{-4}$.

4.3 BR1202−0725 SMG component

4.3.1 Line profiles

The [C II] and CO ($J = 5 \to 4$) spectra for the BR1202−0725 SMG are shown in Fig. 8. Whilst the previous line profiles have all been roughly Gaussian in nature, the [C II] emission line has a much more perturbed shape, with n_{max} of 5 required to adequately describe it with an FWHM of 700 ± 21 km s^{-1}. The CO line however is simply described by a single Gaussian with an FWHM of 970 ± 90 km s^{-1}, such that as with the QSO the CO ($5 \to 4$) line is approximately 30 per cent broader than the [C II].

4.3.2 Performing a joint fit

The evidence heavily favours two independent line shapes, with a difference in the log evidence of 20, corresponding to a probability of >99.99 per cent that the emission lines do not share the same profile. Due to the non-Gaussian nature of their shape, comparing the line centroids for independent models makes little sense, as the centres are at that stage largely arbitrary; however, forcing a single profile upon the pair we find a best fit described by n_{max} of 3, with an FWHM of 700 ± 26 km s^{-1} shown in Fig. 9 (left). Line centroids and redshifts are given in Table 3, and correspond to values of $\Delta z = (-2.0 \pm 1.2) \times 10^{-3}$ as shown in Fig. 9 (right). Once again assuming this change in redshift is the result of only an evolution in the fundamental constants, $\Delta F/F = (-3.5 \pm 2.0) \times 10^{-4}$. The results of the marginalization process are shown in Fig. 10. The posterior for Δz displays a large number of distinct peaks resulting from the irregular line shapes producing a large number of likely models across a range of Δz. We take the most Gaussian-like region to represent our 99 per cent confidence interval for Δz of -1.1 ± 1.5.

5 DISCUSSION

5.1 Spatial distributions of CO and [C II]

When calculating the variation in F by comparing the line centroids of different species, one of the most important considerations is whether or not those two species have the same spatial distribution
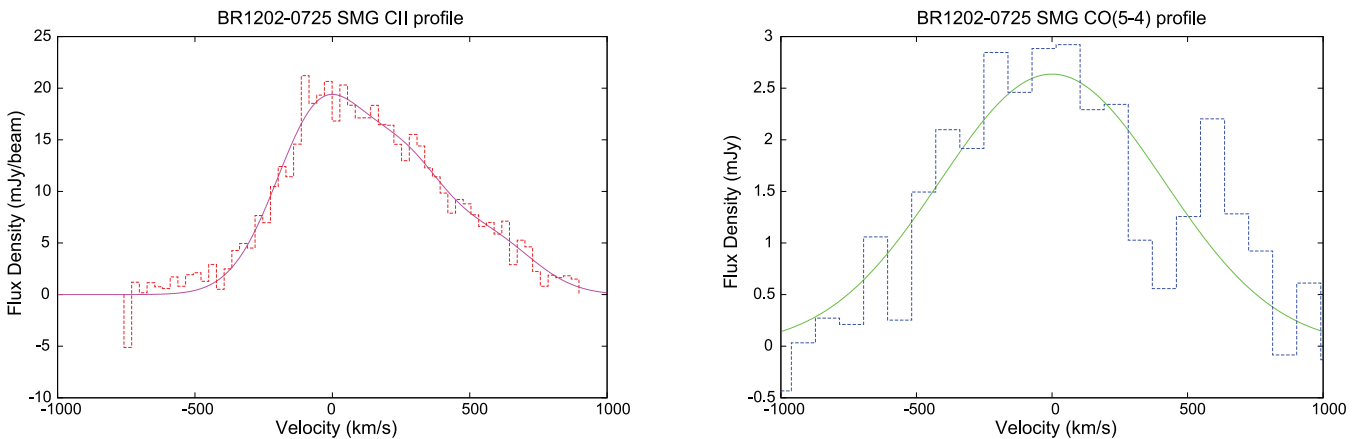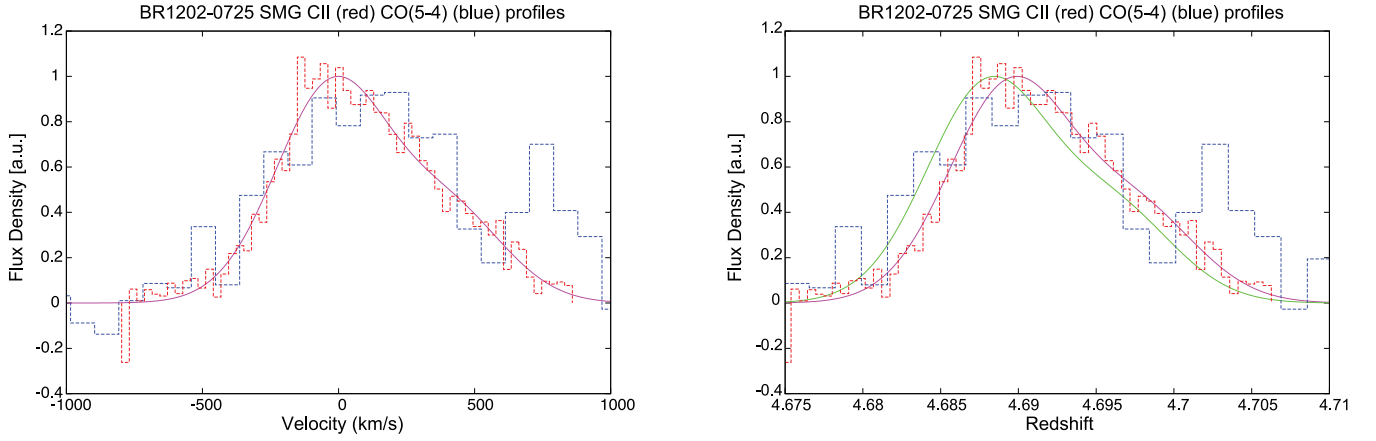

Figure 8. Left: the [C II] spectrum (red dashed) with the best-fitting model (solid magenta) overlaid. Right: CO ($5 \to 4$) spectrum (blue dashed) with the best-fitting model (solid green) overlaid. In both cases, zero velocity is considered to be at the peak of the model.

Figure 9. Left: the best-fitting joint fit profile (solid magenta) overlaid on to both the C ɪɪ (red dashed) and CO $(5 \rightarrow 4)$ (blue dashed) emission lines. Amplitudes have been normalized such that the model has a peak at 1.0, whilst the CO $(5 \rightarrow 4)$ and C ɪɪ emission lines have peaks normalized such that their height relative to the model is as in the best fit. Right: C ɪɪ data (red dotted line) and CO $(5 \rightarrow 4)$ data (blue dotted line) on a redshift axis with amplitudes normalized as in the left-hand panel. The solid magenta and green lines denote the joint fit model line profile at the best-fitting redshift values for the C ɪɪ and CO $(5 \rightarrow 4)$ lines, respectively.

Table 3. BR1202−0725 SMG emission line parameters from a joint fit.

Line	ν_{obs} (GHz)	z
[C ɪɪ]	333.762 ± 0.009	$4.694\,29 \pm 0.000\,16$
CO $(5 \rightarrow 4)$	101.236 ± 0.022	4.6923 ± 0.0012

within the host galaxy. Recent high-resolution studies (∼50 pc scale) of star-forming regions in M33 (Mookerjea et al. 2011) have shown that the CO $(J = 2 \rightarrow 1)$ emission line is shifted by $+1.6$ km s^{-1} relative to the [C ɪɪ]. These authors find that significant parts of the [C ɪɪ] are not traced by the CO because the latter is photodissociated in the low-metallicity environment of M33. Rodriguez-Fernandez et al. (2006) compared [C ɪɪ] and CO emission on the scale of ∼300 pc in the spiral arms of M31 and find that whilst overall they trace the same regions, their maxima are not coincident, with the tighter correlation being between the [C ɪɪ] and

Hα, i.e. tracers of star formation. As such, below 300 pc we are not justified in assuming that the two species co-exist spatially.

Unresolved comparisons of [C ɪɪ] and CO (see e.g. Stacey et al. 1991) however have shown good agreement between line profiles on ∼ kpc scales. Our comparison of the [C ɪɪ] and CO $(J = 2 \rightarrow 1)$ for J1148+5251 showed that there is a 76 per cent probability that the two emission lines share the same profile, indicating that at least on large scales they may indeed trace out the same spatial volume.

For the BR1202−0725 QSO and SMG however, we found ∼65 and >99.9 per cent probabilities that the CO $(J = 5 \rightarrow 4)$ and [C ɪɪ] emission lines have different intrinsic profiles. In both cases, the CO $(J = 5 \rightarrow 4)$ was approximately 30 per cent wider than the [C ɪɪ], which suggests that even on large scales the spatial distribution of these two species is not coherent. We therefore see that with individual systems showing such discrepancies, any one estimate of Δz from a single source will inherently have some unknown error associated with offsets in the distribution of the two species of gas.

Several physical explanations exist to explain such variations. Compact starburst regions can be optically thick in CO, but thin in [C ɪɪ], and hence the CO line only samples the outer regions of the
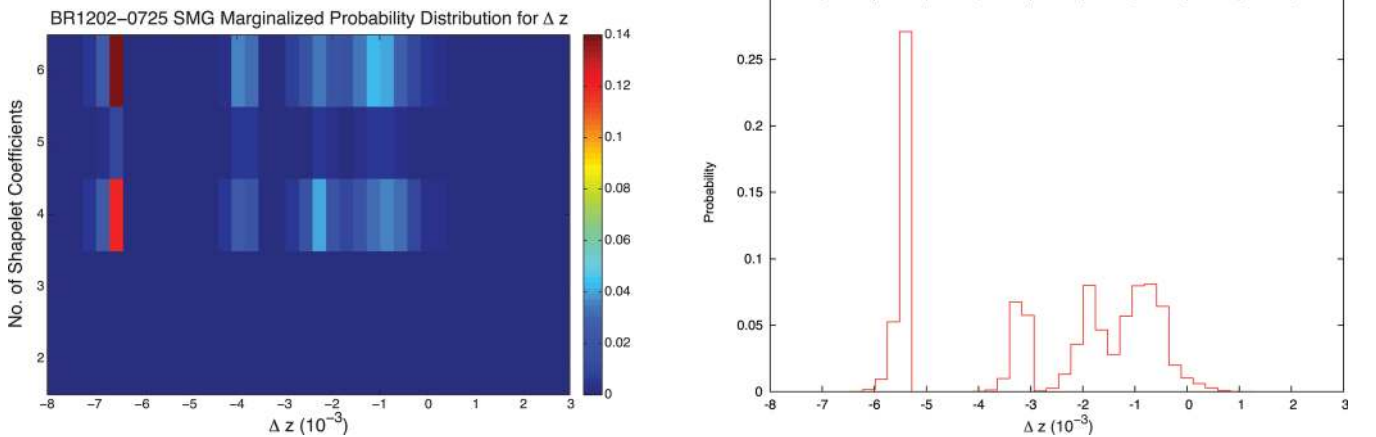

Figure 10. Left: normalized 2D probability distribution for n_{max} and Δz marginalized over shapelet coefficients. Right: normalized 1D probability distribution for Δz marginalized over all n_{max} and all shapelet coefficients.

galaxy leading to larger line widths for the CO relative to [C II]. Conversely, the dust emission in such regions can become optically thick in the rest-frame FIR (at the frequency of the [C II] line), reducing its intensity. Both [C II] and CO emission have been observed in the photon-dominated regions of molecular clouds (Hollenbach & Tielens 1999). Models suggest a separation in the two species, with [C II] tracing the outer layers of molecular clouds and CO emission coming from within. Observations of the warm interstellar medium in the Galaxy (Velusamy et al. 2012) have also shown that [C II] traces a larger region than the CO.

5.2 The evolution of the fundamental constants

Table 4 summarizes our results for $\Delta F/F$ for both approaches – calculating the single joint model that maximizes the evidence, and marginalizing over all possible models. Errors for the single fit are given as 3σ values, whilst the result for marginalizing over the posterior is given as a 99 per cent confidence interval.

Our value of $\Delta F/F$ for J1148+5251 of $-3.3 \pm 2.3 \times 10^{-4}$ is the result of a velocity offset with a 99 per cent confidence interval of 99 ± 69 km s^{-1}. Thus, in order to account for the offset from zero we would require that either the interstellar medium has an intrinsic velocity dispersion much greater than expected or the two species are positioned in such a way that their profiles are consistent, but their relative velocities are significantly offset. From Fig. 2, we can see that the data obtained for the CO $(2 \to 1)$ line only just extend beyond the width of the line. There is the possibility then that the baseline level for this emission line has an additional component that is not easily visible from the data. We therefore allowed the continuum component of the [C II] and CO lines to vary independently for J1148+5251 to see how this affected the outcome of the fit. The result was that it did not. The [C II] and CO fitted continuum components of $+0.43 \pm 0.37$ and $+0.008 \pm 0.009$, respectively, with $\Delta F/F = (-3.3 \pm 0.8) \times 10^{-4}$ as before.

For the BR1202−0725 QSO our value for $\Delta F/F$ of $(-5 \pm 15) \times 10^{-5}$ results from a velocity offset of 15 ± 45 km s^{-1}, which is consistent with our estimates of the intrinsic velocity dispersion of the two species.

Finally, for the BR1202−0725 SMG the best-fitting model we found gave a velocity offset of -120 ± 60 km s^{-1}, whilst the marginalized posterior had multiple peaks between -375 and $+30$ km s^{-1}. This is the result of attempting to fit a joint model to the two emission lines where the evidence strongly favours different profiles for each. We note that the range of the offset in velocity seen in the marginalized posterior is roughly consistent with the difference in the widths of their profiles when fitted independently ($\sim$300 km s^{-1})

If we want to reach a limit of $\Delta F/F < 10^{-6}$ using CO and [C II], we will therefore need to sample large numbers of high-z objects in order to reduce the error associated with the random motions of the gas to $\sim$0.3 km s^{-1} and address other factors such as differing (both gas and dust) opacities. To go from even a modest estimate

of this random motion of 10 km s^{-1} would require $\sim$1000 sources, assuming Gaussian statistics. Alternatively, spatially resolved imaging could be performed on a number of sources, thereby providing multiple, independent line-of-sight measurements for each source. We could also choose to use two species whose spatial distributions are believed to be more closely tied, but that are still detectable with high signal-to-noise ratio at comparable look-back times; for example, Weiß et al. (2012) use a combination of C I and CO $(7 \to 6)$ emission from a $z = 2.79$ QSO host galaxy to derive limits on $\Delta F/F$ of $6.9 \pm 3.7 \times 10^{-6}$.

Finally, if we compare our results to the proposed angular dipole distribution (Webb et al. 2011; King et al. 2012), J1148+251 lies in a region with $\cos\theta \sim -0.9$ with θ the angular separation with respect to the dipole, and so we would expect $\Delta\alpha/\alpha \sim -0.9 \times 10^{-5}$. Given $\Delta F/F = 2\Delta\alpha/\alpha - \Delta\mu/\mu$, if we take $\Delta\mu/\mu = 0$, we find $\Delta\alpha/\alpha = (-1.8 \pm 1.2) \times 10^{-4}$ which is consistent with the value predicted by the dipole. BR1202−0725 however lies almost orthogonal to the dipole with $\cos\theta \sim 0.2$ and so does not produce any stringent tests on the claim.

5.3 The origin of Δz

Out of the three systems investigated, only the [C II] and CO $(J = 2 \to 1)$ transition lines from J1148+5251 were seen to be consistent with one another within the limits of the data; however, we note that the CO $(J = 2 \to 1)$ emission line also had the lowest signal-to-noise ratio of any of the data presented here. The CO $(J = 5 \to 4)$ and [C II] emission lines from the BR1202−0725 QSO and SMG however were both seen to have intrinsically different profiles, where in both cases the CO $(J = 5 \to 4)$ was approximately 30 per cent wider than the [C II]. As such we propose that for individual systems the differences in the redshifts Δz of the CO and [C II] emission lines cannot be viewed as being solely due to the evolution of the fundamental constants, but must include a contribution owing to the intrinsically different spatial distributions of the two species of gas within the galaxy.

6 CONCLUSIONS

We have presented a series of sensitive observations of molecular CO and [C II] emission in three high-redshift galaxies: the QSO host J1148+5251 at $z = 6.4$ and the QSO host BR1202−0725 at $z = 4.7$ along with its companion SMG. We have used these to quantify the differences in the two emission line profiles for each system and thus put constraints on the quantity $\Delta z = z_{CO} - z_{C II}$ in two distinct ways: calculating the Bayesian evidence for a joint model using shapelets and determining the separation in redshift between those models, and marginalizing over all model parameters to calculate the posterior distribution associated with Δz independent of any particular model choice.

We found that the line profiles for the CO $(5 \to 4)$ transition for the BR1202−0725 QSO and SMG were inconsistent with the

Table 4. Final derived values for $\Delta F/F$.

System	$\Delta F/F$ Single joint fit $\pm$ (3σ errors)	Marginalized result (99 per cent confidence interval)
J1148+5251	$(-3.6 \pm 2.4) \times 10^{-4}$	$(-3.3 \pm 2.3) \times 10^{-4}$.
BR1202−0725 QSO	$(-5 \pm 15) \times 10^{-5}$	$(-5 \pm 15) \times 10^{-5}$
BR1202−0725 SMG	$(-4 \pm 6) \times 10^{-4}$	$(-4 \pm 6) \times 10^{-3}$

[C II], being approximately 30 per cent wider whereas the CO (2 → 1) and [C II] emission lines for J1148+5251 were consistent within the limits of the data. This suggests that, in agreement with existing high-resolution observations, whilst the CO and [C II] might largely trace the same components of the host galaxy, there are still observable differences between their line profiles. As such a direct conversion from Δz to the quantity $\Delta F/F$ in order to constrain the evolution of fundamental constants for an individual system using these two species of gas is problematic, with our results being fundamentally limited by this unknown factor that represents the relative distributions and velocities of the gas within the host galaxy. Such issues are potentially eliminated either with large sample sizes to reduce the random error or by observing different species that are more closely linked. In either case, the sensitivity of ALMA will allow large numbers of CO and [C II] detections at high redshift to mitigate the issue, allowing us to reduce the uncertainty in the evolution of the fundamental constants at these distant look-back times to the level of $\sim 10^{-6}$, on a par with methods used at lower redshifts.

ACKNOWLEDGEMENTS

REFERENCES

Agafonova I. I., Molaro P., Levshakov S. A., Hou J. L., 2011, A&A, 529, A28
Berry R. H., Hobson M. P., Withington S., 2004, MNRAS, 354, 199
Crawford M. K., Genzel R., Townes C. H., Watson D. M., 1985, ApJ, 291, 755
Dirac P. A. M., 1937, Nat, 139, 323
Feroz F., Hobson M. P., Bridges M., 2009, MNRAS, 398, 1601
Hollenbach D. J., Tielens A. G. G. M., 1999, Rev. Mod. Phys., 71, 173
Kanekar N., 2011, ApJ, 728, L12
Kanekar N., Langston G. I., Stocke J. T., Carilli C. L., Menten K. M., 2012, ApJ, 746, L16
Kelly B. C., McKay T. A., 2004, AJ, 127, 625
Kelly B. C., McKay T. A., 2005, AJ, 129, 1287
King J. A., Webb J. K., Murphy M. T., Flambaum V. V., Carswell R. F., Bainbridge M. B., Wilczynska M. R., Koch F. E., 2012, MNRAS, 422, 3370
Levshakov S. A., Reimers D., Kozlov M. G., Porsev S. G., Molaro P., 2008, A&A, 479, 719
Levshakov S. A., Combes F., Boone F., Agafonova I. I., Reimers D., Kozlov M. G., 2012, A&A, 540, L9
Maiolino R. et al., 2012, MNRAS, 425, L66
Milne E. A., 1935, Relativity, Gravitation and World-Structure. Clarendon Press, Oxford
Mookerjea B. et al., 2011, A&A, 532, A152
Refregier A., 2003, MNRAS, 338, 35
Refregier A., Bacon D., 2003, MNRAS, 338, 48
Rodriguez-Fernandez N. J., Braine J., Brouillet N., Combes F., 2006, A&A, 453, 77
Salome P., Guelin M., Downes D., Cox P., Guilloteau S., Omont A., Gavazzi R., Neri R., 2012, A&A, 545, A57
Stacey G. J., Geis N., Genzel R., Lugten J. B., Poglitsch A., Sternberg A., Townes C. H., 1991, ApJ, 373, 423
Uzan J.-P., 2011, Living Rev. Relativ., 14, 2
Velusamy T., Langer W. D., Pineda J. L., Goldsmith P. F., 2012, A&A, 541, L10
Wagg J. et al., 2012, ApJ, 752, L30
Webb J. K., King J. A., Murphy M. T., Flambaum V. V., Carswell R. F., Bainbridge M. B., 2011, Phys. Rev. Lett., 107, 191101
Weiß A., Walter F., Downes D., Carrili C. L., Henkel C., Menten K. M., Cox P., 2012, ApJ, 753, 102

This paper has been typeset from a TeX/LaTeX file prepared by the author.